scientific reports

Check for updates

OPEN

Near dipole-dipole interaction induced control of high-precision three-dimensional atom localization via probe absorption in a four-level phase-coherent atomic medium

Aniket Banerjee[1,2], Pradipta Panchadhyayee[2,3,4,6]✉ & Bibhas Kumar Dutta[5,6]✉

It is newly proposed that the presence of the near dipole-dipole (NDD) interaction effect in an optically dense atomic ensemble may be very useful for controlling high-precision atom localization. In the present work based on observing the NDD effect-induced space-dependent-absorption of a weak probe field operating in a partially closed four-level Y-type atomic system, we have shown the NDD parameter being an efficient control knob along with the other system parameters for easier optimization of the localization pattern with enhanced detection probability in three-dimensional (3D) space. Controlling localization patterns at lower and larger values of NDD parameter is discussed at different physical conditions. In the present model, we mention that the maximum detection probability of the atom is found with the spatial resolution limit having localization volume nearly of the order of $(\lambda/100)^3$. The efficacy of the present model is in finding its application in atom nanolithography and atom imaging, which are important for quantum information processing and technology.

The study on high-precision atom localization is beneficial for its potential applications in laser cooling and trapping of neutral atoms[1,2], Bose–Einstein condensation[3,4], measurement of center-of-mass wave function[5], and atom nanolithography[6,7]. In contrast to the previous mechanism[8–11] of measurement-induced localization procedure based on measuring the phase shift of off-resonant standing waves interacting with the atom, many authors have subsequently employed different techniques using coherent control of opto-atomic properties at resonant atom-field coupling within the standing-wave regime to demonstrate one-dimensional (1D) atom localization in the subwavelength domain[12–21]. Such as, the properties of 1D atom localization were explained by observing atomic state-population by Paspalakis and Knight[12] in a three-level atomic model controlled by quantum interference, and then the process followed by Agarwal and Kapale[18] in a similar model at the condition of coherent population trapping (CPT). In different atomic configurations, the method of probing spatially modulated fluorescence, linear absorption and Raman-gain were put forward by Zubairy and his group[14,15] and Qamar et al.[17], respectively, to investigate 1D atom localization. The influence of double dark resonances on the localization behaviour was shown by Liu et al.[16]. Qamar et al.[13] introduced the process of visualizing 1D atom localization via steady-state resonance fluorescence. Proite et al.[19] provided experimental evidence of 1D localization patterns as a result of electromagnetically induced transparency (EIT). Wang and Jiang[20] and Dutta et al.[21] have analyzed the manipulation of localization peaks in the sub-half-wavelength domain through probe absorption in different atomic systems. In addition to 1D atom localization, two-dimensional (2D) atom

[1]Department of Physics (UG and PG), Panskura Banamali College (Autonomous), Purba Medinipur, W. B. 721152, India. [2]Research Centre in Natural Sciences, Prabhat Kumar College, Contai (Vidyasagar University), Purba Medinipur, W. B. 721401, India. [3]Department of Physics (UG and PG), Prabhat Kumar College, Contai (Vidyasagar University), Purba Medinipur, W. B. 721401, India. [4]Institute of Astronomy Space and Earth Science, Kolkata, W. B. 700054, India. [5]Department of Physics, Sree Chaitanya College, Habra (WB State University), North 24 Parganas 743268, W. B., India. [6]Bibhas Kumar Dutta and Pradipta Panchadhyayee contributed equally to this work ✉email: pradipta@pkcollegecontai.ac.in; bibhas_k_dutta@yahoo.co.in

localization resulting from the simultaneous interaction of an atom with two orthogonal standing-wave fields was predicted by Evers et al.[22]. Gong and his team[23] elaborated the study on 2D localization to exhibit its importance in atom nanolithography. After that, several techniques[24–43] have been utilized to obtain 2D atom localization, which are briefly mentioned as follows: analyzing conditional position probability of excited-state atomic population in the case of EIT by Ivanov and Rozhdestvensky[24] and Wang et al.[38]; using position-dependent Autler–Townes microscopy by Shui et al.[37]; investigating spatially modulated probe absorption by Ding et al.[25,30], Rahmatullah and Qamar[34], Wu et al.[35] and Idrees et al.[40], and analogously studying space-dependent probe-transmission spectrum by Idrees et al.[41,42]; probing position-dependent spontaneous emission spectra by Gao and his colleagues[26,27], Ding et al.[29,32], Li et al.[31] and Wang et al.[33]; observing position-dependent resonance fluorescence spectrum by Dutta et al.[39]. The role of double dark resonances and spontaneously generated coherence (SGC) in manipulating 2D localization patterns have been reported by Wan et al.[28] and Shui et al.[36], respectively. An attempt has been made to exhibit 2D atom localization theoretically by observing position-dependent absorption of surface plasmon polariton (SPP) generated at the interface between metal (*Ag*) and dielectric medium (^{87}*Rb vapour*)[43].

Besides 2D atom localization, the coherent interaction of an atom with three orthogonal standing wave fields makes it possible to achieve three-dimensional (3D) atom localization. Similar techniques used to obtain 2D localization patterns were exploited by different authors[44–61] to demonstrate theoretically the 3D atom localization. As the study of 3D atom localization is the primal objective of the present work, we specify the basics of the earlier works on 3D localization in the following. Qi et al.[44] explored subwavelength 3D atom localization by measuring space-dependent probe absorption guided by EIT in a five-level M-type atomic system. Ivanov et al.[45] reported various 3D localization patterns in a four-level Tripod-type scheme by observing the upper-state population. However, these two studies[44,45] did not show any improvement in the maximum detection probability of an atom in 3D space. Wang and Yu[46] proposed a scheme for 3D localization based on probe absorption in a three-level scheme to predict 100% detection probability of atom. Subsequent works[47,49–61] reflected similar features in the 3D localization patterns. Zhu et al.[49] employed a three-wave mixing technique in a V-type three-level atom to achieve 3D localization. Yang et al.[52] illustrated 3D atom localization in the sub-half-wavelength domain through interacting double dark resonances. By measuring phase-dependent spatially modulated absorption with a variety of atom-field configurations, control of precise position information of atom in 3D space is noted in the works performed by Hamedi and Mehmannavaz[48], Wang et al.[54], Mao and Wu[55], Zhang et al.[57,60], and Song et al.[61]. The study of 3D atom localization by analyzing the atomic population in the excited states was carried out by Zhu et al.[51] in a double two-level atomic system and Wang and Yu[53] in a closed four-level double-Λ system. Panchadhyayee et al.[58] proposed a model based on resonance fluorescence microscopy to obtain 3D atom localization with 100% detection probability in the sub-half-wavelength domain. 3D localization patterns based on probing position-dependent spontaneous emission spectra in different multilevel atomic systems were discussed by Wang and Yu[50], Chen et al.[56], and Song et al.[59]. The limit of spatial resolution of the localized atom is predicted as 0.04λ in Ref.[59].

We summarize the techniques behind 1D, 2D, and 3D atom localizations as raised in the above paragraphs. It will be noticeable that most of the authors have undertaken the measurement of spatially modulated probe absorption because of its straightforward implementation in experiments. In this article, we are also interested in the study of 3D atom localization based on the method of observing position-dependent probe absorption in a partially closed four-level Y-type atomic system (Fig. 1a). But, in contrast to the previous works[54,55,57,60,61] on 3D localization, the NDD effect[62,63] induced modified-susceptibility of probe transition has been taken into account in the present model. The reason behind such a study is stated as follows. Under the condition of considerable

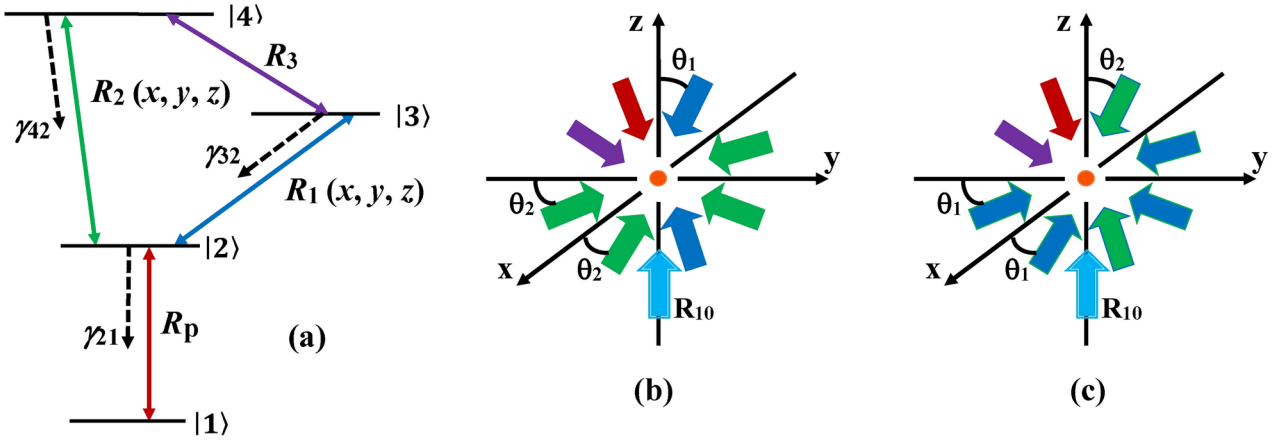

Fig. 1. (**a**) Field-coupled energy level diagram of a partially closed four-level *Y*-type atomic model. The probe field (R_p) is applied to the $|1\rangle$ - $|2\rangle$ transition. $R_1(x, y, z)$, and $R_2(x, y, z)$ represent the Rabi frequencies of two space-dependent control fields, which are applied to the respective transitions, $|2\rangle$ - $|3\rangle$ and $|2\rangle$ - $|4\rangle$. A radio-frequency field of Rabi frequency R_3 is applied to the $|3\rangle$ - $|4\rangle$ transition. (**b**) and (**c**) are presented for the schematic diagrams corresponding to the Schemes I, and II (see text), respectively. The orange circle in the plots (**b**) and (**c**) denotes the atom.

atomic density ($\approx 10^{12}$-10^{15} atoms/cm^3), there may be many atoms within a cubic resonance wavelength of the probe field, because of which one cannot ignore the significant role of NDD effect in modulating the probe response strongly, as has been manifested in the earlier works to exhibit the formation of modified coherence effect like inversionless gain accompanied by the enhancement of refractive index[63,64] and the manipulation of band-gap[65] in optically dense atomic systems. Motivated by the interesting outcomes of these works, we set our objectives to examine the generation of 3D localization patterns by including the NDD effect in our theoretical model. After a short while, it will be shown that the NDD effect causes a dramatic change in the 3D localization patterns obtained without invoking this effect. More specifically, the localization pattern obtained by a particular setting of system parameters, like Rabi frequency, detuning, and collective phase, can be altered into a new one for a specific value of the NDD parameter. Thus, the NDD effect makes it possible to modify significantly the detection efficiency of high-precision atom localization in 3D space with small adjustments of values of other system parameters. Herein lies the uniqueness of the methodology considered for the present work when compared to the earlier ones.

In the given model (Fig. 1a), for the space-dependent control fields of Rabi frequencies $R_j(x, y, z)$ $(j = 1, 2)$ along with the radio-frequency field of Rabi frequency R_3, position information of the atom is obtained via probe absorption in two different schemes (Fig. 1b,c) owing to the variation of standing-wave field configurations. In one scheme, we set $R_1(z)$ and $R_2(x, y)$ *i.e.* the consideration of standing wave along z-direction is for the control field of Rabi frequency R_1 and the other standing waves along the x- and y- directions are for the control field of Rabi frequency R_2. A travelling wave is accompanied by the z-directional standing wave. In another scheme, two standing waves along the x- and y- directions are taken into consideration for the control field of Rabi frequency R_1. Here, $R_1(x, y)$ is applied to the system with the association of a travelling wave field. We consider $R_2(z)$ as the z-directional standing wave. In the following, salient features of the present work are discussed briefly.

In both the schemes, at lower values of the NDD parameter, 100% detection probability of atom is shown to be easily achievable at specific values of Rabi frequency of the travelling-wave field when all the fields operating in the system are at exact resonance. The spatial resolution of a single 3D structure is optimized by varying the value of the collective phase parameter. While at larger values of the NDD parameter, the value of probe detuning needs to be adjusted to display the regular shapes of 3D structures before setting the value of the Rabi frequency of the travelling-wave field. Then, by varying the value of the phase parameter, the 50% detection probability of the atom can be found with ultra-high spatial resolution. After that, by making proper tuning of the value of Rabi frequency of the travelling-wave field, 100% detection probability of atom is obtained with satisfactory spatial resolution. This behaviour is specific to the given model. In the present model, our results highlight that the maximum detection probability of the atom is attainable with a spatial resolution-limit having the minimum localization volume of the order of $\frac{\lambda^3}{13.6\times10^6}$, where the reference volume is considered as a cube with a side of one wavelength. To our knowledge, no work has been found in the literature on controlling atom localization using the NDD effect. This type of localization control mechanism is specific to the present work.

Theoretical model

The field-coupled energy-level configuration of our four-level scheme is shown in Fig. 1a, where the dipole allowed transitions $|1\rangle$-$|2\rangle$, $|2\rangle$-$|3\rangle$ and $|2\rangle$-$|4\rangle$ are guided by three coherent fields. The transition from $|1\rangle$ to $|2\rangle$ is governed by a weak probe field of Rabi frequency R_p. A radio-frequency field of Rabi-frequency R_3 is applied in the system to couple the energy levels $|3\rangle$ and $|4\rangle$. Each of the two control fields driving the transitions $|2\rangle$-$|3\rangle$ and $|2\rangle$-$|4\rangle$ is comprised of one or more orthogonal standing waves with a variety of combinations. So, their Rabi frequencies are generally designated as $R_1(x, y, z)$ and $R_2(x, y, z)$ in Fig. 1a. It should be mentioned here that $R_1(x, y, z)$ is always accompanied by a constant Rabi frequency R_{10} of a travelling-wave field applied in the transition $|2\rangle$-$|3\rangle$. For various combinations of different standing wave field configurations in different transitions, we have considered two different schemes I and II as shown in Fig. 1b,c, respectively. The field configuration is expressed for the scheme—I as

$$\begin{aligned} R_1(z) =& R_{10} + R_1 sin(k_1 cos(\theta_1)z + \varphi_1), \\ R_2(x, y) =& R_2(sin(k_2 cos(\theta_2)x + \varphi_2) + sin(k_2 cos(\theta_2)y + \varphi_2)) \end{aligned} \tag{1}$$

and for the scheme -II as

$$\begin{aligned} R_1(x, y) =& R_{10} + R_1(sin(k_1 cos(\theta_1)x + \varphi_1) + sin(k_1 cos(\theta_1)y + \varphi_1)), \\ R_2(z) =& R_2 sin(k_2 cos(\theta_2)z + \varphi_2) \end{aligned} \tag{2}$$

Here, φ_1 and φ_2 are the phase shifts of the corresponding standing-wave fields. Without loss of generality, we represent $k_1 cos(\theta_1) = k\eta_1 cos(\theta_1)$ and $k_2 cos(\theta_2) = k\eta_2 cos(\theta_2)$, where the factor η_j $(j = 1, 2)$ appears due to a small difference in magnitude of k_1 and k_2. We mention that the term defined as $k\eta_j cos(\theta_j)$ is more explicit when compared to the similar term considered in Ref.[40–42] on the exclusion of 'cosine'-term in presenting the mathematical form of standing wave. For the sake of simplicity of the model, we need to point out that, by adjusting the values of θ_1 and θ_2, it is possible to make the product-terms $\eta_1 cos(\theta_1)$ and $\eta_2 cos(\theta_2)$ to be almost equal. This enables us to consider $k_1 cos(\theta_1) \approx k_2 cos(\theta_2) = k$ for the purpose of numerical computation.

It is assumed that the center of mass of the atom is at rest during the resonant interaction of the atom with the standing wave fields. Then, we neglect the transverse kinetic energy of the atom as it becomes very much smaller than the atom-field interaction energy in the standing wave regime. Thus, the expression of the Hamiltonian

will not contain any kinetic energy term under the Raman-Nath approximation[66]. The coherent part of the interaction Hamiltonian of the system can be written as (Appendix - See Supplementary Information)

$$\mathcal{H} = -\hbar[-\Delta_p|2\rangle\langle 2| - (\Delta_p + \Delta_1)|3\rangle\langle 3| - (\Delta_p + \Delta_2)|4\rangle\langle 4| + (|R_p||2\rangle\langle 1| + |R_1(x,y,z)||3\rangle\langle 2| + |R_2(x,y,z)||4\rangle\langle 2| + |R_3|e^{i\phi}|4\rangle\langle 3| + H.c.)] \tag{3}$$

In the following part of the present section and the other sections, the magnitudes of the Rabi frequencies will be denoted as simply R_j.

The system dynamics can be explained by the semiclassical density matrix equation as given by

$$\frac{\partial \rho}{\partial t} = -\frac{i}{\hbar}[\mathcal{H}, \rho] + \Lambda\rho \tag{4}$$

where the term $\Lambda\rho$ includes the effect of incoherent decay-mechanism inherent to the present model. In the following, $\Lambda\rho$ is explicitly expressed as

$$\begin{aligned}\Lambda\rho =& \frac{\gamma_{21}}{2}[2|1\rangle\langle 2|\rho|2\rangle\langle 1| - |2\rangle\langle 2|\rho - \rho|2\rangle\langle 2|] \\ &+ \sum_{j=3,4} \frac{\gamma_{j2}}{2}[2|2\rangle\langle j|\rho|j\rangle\langle 2| - |j\rangle\langle j|\rho - \rho|j\rangle\langle j|]\end{aligned} \tag{5}$$

Now, the required off-diagonal density matrix equations are presented as follows

$$\dot{\rho}_{21} = -Z_2\rho_{21} + iR_p(\rho_{11} - \rho_{22}) + iR_1(x,y,z)\rho_{31} + iR_2(x,y,z)\rho_{41}, \tag{6}$$

$$\dot{\rho}_{31} = -Z_3\rho_{31} - iR_p\rho_{32} + iR_1(x,y,z)\rho_{21} + iR_3e^{-i\phi}\rho_{41}, \tag{7}$$

$$\dot{\rho}_{41} = -Z_4\rho_{41} - iR_p\rho_{42} + iR_2(x,y,z)\rho_{21} + iR_3e^{i\phi}\rho_{31} \tag{8}$$

where $Z_2 = \frac{\gamma_{21}}{2} + i\Delta_p$, $Z_3 = \frac{\gamma_{32}}{2} + i(\Delta_p + \Delta_1)$ and $Z_4 = \frac{\gamma_{42}}{2} + i(\Delta_p + \Delta_2)$. γ_{jk} $(jk = 21, 32, 42)$ denotes the natural decay rate.

Under the weak-probe-field approximation, we treat the Rabi frequency R_p to the first order, and other Rabi frequencies to all orders to solve the given set of density matrix equations to obtain the expression of ρ_{21}. For $\rho_{11} \approx 1$, ρ_{21} can be presented as

$$\rho_{21} = \frac{iR_p(Z_3Z_4 + R_3^2)}{A + R_1^2(x,y,z)Z_4 + R_2^2(x,y,z)Z_3 + 2iR_1(x,y,z)R_2(x,y,z)R_3cos(\phi)}, \tag{9}$$

where $A = Z_2Z_3Z_4 + R_3^2Z_2$. In the denominator of the expression (9), the fourth term relating to the product of the Rabi frequencies represents the interference effect appearing in the given model.

The polarization induced in the probe transition is given by performing the quantum average over the corresponding transition moment[66] as follows

$$\mathcal{P} = \epsilon_0\chi\epsilon_p = 2N\mu_{12}\rho_{21}, \tag{10}$$

where ϵ_0 being the free-space permittivity and N the atomic density. The macroscopic susceptibility $\chi(x,y,z)$ is expressed as

$$\chi(x,y,z) = C\chi_o(x,y,z) \tag{11}$$

with $C = \frac{N|\mu_{12}|^2}{\epsilon_0\hbar\gamma_{21}}$ as the dimensionless constant[63] and the microscopic susceptibility

$$\chi_o(x,y,z) = \frac{\gamma_{21}\rho_{21}(x,y,z)}{R_p} \tag{12}$$

C is equivalent to the weight factor of the optical density of the medium related to the susceptibility of probe response. For the sake of simplicity of the calculation, C is chosen to be unity. We mention that $Im(\chi_o)$ and $Re(\chi_o)$ correspond to probe absorption and dispersion evolved in the system, respectively[67].

Modified macroscopic-susceptibility under NDD effect: In general, in a linear, homogeneous, and isotropic dielectric substance with uniformly arranged tiny dipoles under the influence of external electric field, as a consequence of the phenomenon of NDD interaction the effective (termed as '*Local*') microscopic field $\bar{E}_L$ experienced by any of the dipoles is expressed by the Lorentz relation[68] as

$$\bar{E}_L = \bar{E} + \frac{\bar{P}}{3\epsilon_0}, \tag{13}$$

where $\bar{E}$ stands for the macroscopic field and $\bar{P}$ denotes the volume-polarization of the dipoles. In an optically dense atomic medium, such consideration of *Local* field is equally applicable to any atom taken as point-dipole in the atomic ensemble. Keeping in mind such physical situation, it is imperative to mention here that, for a multi-

level atomic system interacting with the coherent fields, the appearance of the NDD effect leads us to consider the *Local* field correction in defining the macroscopic susceptibility relating to probe-transition. To this aim, we have followed the generalized approach as described in Ref.[62] for incorporating *Local* field correction in a two-level atomic model and the direct way of implementing it to represent the macroscopic polarization induced by a probe field in a three-level atomic model[63]. Without repeating further the detailed process of the required derivation, we briefly outline the following points. Firstly, if we define the field components in time-varying case as $\bar{E}(t) = \frac{\bar{\mathcal{E}}}{2}\, e^{i\omega t}$ + *c.c.* and $\bar{P}(t) = \frac{\bar{\mathcal{P}}}{2}\, e^{i\omega t}$ + *c.c.*, then it is plausible to introduce $\bar{E}_L(t) = \frac{\bar{\mathcal{E}}_L}{2}\, e^{i\omega t}$ + *c.c.*. Now, by employing the condition of slowly varying amplitudes $\bar{\mathcal{E}}$, $\bar{\mathcal{P}}$ and $\bar{\mathcal{E}}_L$, it is possible to rewrite the Eq. (13) as[62]

$$\bar{\mathcal{E}}_{\mathcal{L}} = \bar{\mathcal{E}} + \frac{\bar{\mathcal{P}}}{3\epsilon_0} \tag{14}$$

The above equation shows the validity of Lorentz relation in the case of time-varying fields. Secondly, in order to include the contribution of *Local* field in the probe transition, it is customary to replace the Rabi frequency term $|R_p|$ appearing in the expression (3) of the Hamiltonian $\mathcal{H}$ by $|R_L| = \left|\frac{\bar{\mu}_{21}\cdot\bar{\mathcal{E}}_L}{2\hbar}\right|$ with the consideration of $\bar{\mathcal{E}}$ as $\bar{\epsilon}_p$ as similarly noted in Ref.[63]. Accordingly, in the expression (9) of ρ_{21}, R_L (basically $|R_L|$) appears instead of R_p (basically $|R_p|$). Now, it is straightforward to represent the expression of the magnitude of macroscopic polarization as[63]

$$\mathcal{P} = \frac{N|\mu_{12}|^2|\mathcal{E}_L|}{\hbar\gamma_{21}}\chi_o(x,y,z) = \frac{N|\mu_{12}|^2(\epsilon_p + \frac{\mathcal{P}}{3\epsilon_0})}{\hbar\gamma_{21}}\chi_o(x,y,z) \tag{15}$$

with $\chi_o(x,y,z) = \frac{\gamma_{21}\rho_{21}(x,y,z)}{R_L}$. Using the definition of $\mathcal{P} = \epsilon_0\chi\epsilon_p$, we recast the relation (15) in the following form

$$\chi(x,y,z) = C\chi_0(x,y,z) + \frac{C\chi(x,y,z)\chi_o(x,y,z)}{3}, \tag{16}$$

where *C* is already defined after the expression (11). Simplifying the relation (16), we represent the macroscopic susceptibility in the presence of the NDD effect as

$$[\chi]_{NDD}(x,y,z) = \frac{C\chi_o(x,y,z)}{1 - \frac{1}{3}C\chi_o(x,y,z)}, \tag{17}$$

where *C* plays a vital role as the NDD parameter. We note that the expression of $[\chi]_{NDD}(x,y,z)$ is in conformity with the expression of macroscopic susceptibility in probe transition, as found in Ref.[65,67].

Significance of NDD effect in 3*D localization*: We note that, for the purpose of showing 3D atom localization in the absence of the NDD effect, the position information of the atom in 3D space will be obtained by measuring probe absorption proportional to Im[χ_o(x,y,z)]. While in the presence of the NDD effect, we need to observe the probe absorption, which is proportional to Im[$[\chi]_{NDD}$(x,y,z)]. To exhibit qualitatively the effectiveness of introducing the NDD effect in forming the 3D localization structure in a simple way, we redefine the physical entities $\gamma_{21} = 2\Gamma_1$, $\gamma_{32} = \gamma_{42} = 2\Gamma_2$ and $\Delta_p = \Delta$. With respect to the given expressions (1) and (2), we present in a general way R_1(x,y,z) = $R\,\xi_1$(x,y,z) and R_2(x,y,z) = $R\,\xi_2$(x,y,z) with ξ_1(x,y,z) = ($R_{10}/R + \xi_1'$(x,y,z)). By setting the detuning condition $\Delta_1 = \Delta_2 = 0$, the expressions of the imaginary parts of the susceptibilities are given in reduced forms as follows

$$Im[\chi_o(x,y,z)] = \frac{2\Gamma_1(a_1 - \Delta^2)U(x,y,z,\Delta) + 4\Gamma_1\Gamma_2 V(x,y,z,\Delta)\Delta}{U(x,y,z,\Delta)^2 + V(x,y,z,\Delta)^2} \tag{18}$$

with

$$\begin{aligned} U(x,y,z,\Delta) =& a_2(x,y,z) - a_3\Delta^2, \\ V(x,y,z,\Delta) =& (a_4(x,y,z) - \Delta^2)\Delta + a_5(x,y,z), \end{aligned}$$

and

$$\begin{aligned} Im[[\chi]_{NDD}(x,y,z)] =& \frac{2C\Gamma_1(a_1 - \Delta^2)U'(x,y,z,\Delta)}{U'^2(x,y,z,\Delta) + V'^2(x,y,z,\Delta)} \\ &+ \frac{4C\Gamma_1\Gamma_2 V'(x,y,z,\Delta)\Delta}{U'^2(x,y,z,\Delta) + V'^2(x,y,z,\Delta)}, \end{aligned} \tag{19}$$

with

$$U'(x,y,z,\Delta) = U(x,y,z,\Delta) + \frac{4C}{3}\Gamma_1\Gamma_2\Delta,$$
$$V'(x,y,z,\Delta) = V(x,y,z,\Delta) - \frac{2C}{3}\Gamma_1(a_1 - \Delta^2),$$

where $a_1 = \Gamma_2^2 + R_3^2$, $a_2(x,y,z) = \Gamma_1 a_1 + \Gamma_2 R^2(\xi_1(x,y,z) + \xi_2(x,y,z))$, $a_3 = \Gamma_1 + 2\Gamma_2$, $a_4(x,y,z) = a_1 + 2\Gamma_1\Gamma_2 + R^2(\xi_1(x,y,z) + \xi_2(x,y,z))$ and $a_5 = 2R_3R^2\xi_1(x,y,z)\xi_2(x,y,z)cos(\phi)$. We see that the expressions (18) and (19) look similar. Comparing U' and V' with U and V, respectively, it is worth mentioning that the incorporation of the NDD effect in the system introduces the extra terms leading to the resonant-shifting effect of atom-field interaction in the susceptibility of probe transition. This phenomenon occurs not only with the association of probe detuning, but also in the absence of detuned probe field, which is clearly evident from the appearance of the term $\frac{2C}{3}\Gamma_1 a_1$ in V'. This feature implies that even when Δ is set to zero, by varying the strength of NDD parameter C, the equivalence of detuning-induced optimization of localization pattern is attainable in an optically dense atomic ensemble in the presence of NDD effect. From this aspect, the present study is unique when compared to the earlier ones on 3D atom localization based on measuring probe absorption in multi-level atomic systems.

Results and discussions

In the following analysis, we exhibit the variation of the spatially modulated 3D probe absorption of the atom. For two different combinations of field arrangements involving standing-wave and travelling-wave fields, the probe absorption of the system under different parameter conditions is computed using Eqs. (12) and (17) under the steady-state condition. Subsequently, we explore how controlling system parameters can facilitate 3D atom localization and display the changes in space-dependent coherent localization structures in Figs. 2, 3, 4 and 5 in subwavelength and sub-half-wavelength domains. Throughout the whole study, the values of Δ_1 and Δ_2 are considered zero, and the radio-frequency field of Rabi frequency R_3 has no spatial dependence. For the validity of the present model in a real atomic system, we have chosen the hyperfine energy levels of 5*S*, 5*P*, and 5*D* atomic states[69] of ^{87}Rb. Then, the energy eigenstates $|1\rangle$, $|2\rangle$, $|3\rangle$ and $|4\rangle$ are specified as $5S_{1/2}(F=1)$, $5P_{3/2}(F=2)$, $5D_{3/2}(F=1)$ and $5D_{5/2}(F=1)$, respectively. The decay rates γ_{21}, γ_{32}, and γ_{42} are 6 MHz, 0.97 MHz, and 0.97 MHz, respectively. The phase-shift terms (φ_1 and φ_2) appearing in the expressions (Eqs. (1) and (2)) of the standing-wave fields are considered zero in the entire work.

Figure 2 illustrates our investigation on the coherent localization structures corresponding to the 3D probe absorption for the scheme-I. For better comprehension of the impact of the NDD effect on localization isosurfaces in comparison to those in the absence of the NDD effect, we have displayed the localization features in two panels of Fig. 2. Spatial modifications of the coherent localization structures are shown in terms of $Im(\chi_o)$ (following Eq. (12)) in the left panel and $Im([\chi]_{NDD})$ (following Eq. (17)) in the right panel, respectively, for the variation of system parameters. In the scheme-I, where $R_1(z)$ is comprised of one standing-wave field arrangement, while $R_2(x,y)$ corresponds to the spatial field arrangements oriented with the two standing waves. The travelling-wave field R_{10} is associated with $R_1(z)$. For Fig. 2, we set the parameters as: $R_1 = R_2 = 1.6$ MHz, $R_3 = 1.13$ MHz, $\Delta_p = \Delta_1 = \Delta_2 = 0$. To show the NDD-induced variation of isosurface profiles of localization patterns in the right panel of Fig. 2, we set the NDD parameter (C) as 6. Fig. 2a(i) exhibits four oblate spheroids of nearly equal size in the $(\mp x, \mp y, \pm z)$ and $(\pm x, \pm y, \pm z)$ subspaces. These localization patterns are obtained without invoking the travelling-wave field (R_{10}) when the collective-phase parameter (ϕ) becomes zero. The consideration of the NDD effect induces a notable change in the corresponding isosurface profile (Fig. 2a(ii)) when all other parameters remain invariant. Two closely-spaced circular disc-like patterns evolve in the subspaces $(\mp x, \mp y, \pm z)$. When the field (R_{10}) is changed from the 'turned-off' to 'turned-on' condition without considering the NDD effect, two oblate spheroids appearing in the (x, y, z) and $(-x, -y, z)$ subspaces are found to be increased in size (See Fig. 2b(i)). The other two in the $(x, y, -z)$ and $(-x, -y, -z)$ get decreased in comparison to the patterns of Fig. 2a(i). A drastic change in the isosurface profile occurs, in comparison to that for Fig. 2b(i), when the NDD parameter is employed in the model without affecting other parameters. In Fig. 2b(ii), the emergence of one flat disc is exhibited in the $(-x, -y, z)$ subspace with increased thickness. The detection probability of finding the atom in the sub-half-wavelength regime of $(-x, -y, z)$ 3D subspace becomes 100%. For plotting Fig. 2c we set the collective-phase parameter (ϕ) at 0.1755π. Fig. 2c(i) depicts, without considering the NDD effect, how the application of ϕ modifies the localization structures by controlling the coherence of the system. The volumes of the four oblate spheroid-like localization structures decrease when compared to Fig. 2b(i). The distinctive appearance of a tiny, flat, disc-like isosurface is shown in Fig. 2c(ii) under the influence of the NDD effect. By close inspection of Fig. 2c(ii), we observe that the spatial extent of the 3D localization structure is $\Delta(kx/\pi) \approx 0.045$, $\Delta(ky/\pi) \approx 0.03$, and $\Delta(kz/\pi) \approx 0.01$. Thus, the high-precision 3D localization pattern shows the limit of spatial resolution of the order of $\lambda/45$ along the x-direction, $\lambda/67$ along the y-direction, and $\lambda/200$ along the z-direction. Consequently, the degree of localization is estimated in terms of the spatial extent of the localization volume, which appears to be approximately $\frac{\lambda^3}{6\times10^5}$. It can be highlighted that the combined use of the travelling wave and the phase parameter with appropriate values plays a vital role as far as the high-precision atom localization with high resolution is concerned in 3D space.

Next, we have resorted to the scheme-I where the observations on $Im([\chi]_{NDD})$ are reported in Fig. 3 with the consideration of NDD interaction ($C = 9$) in the system. To investigate the salient features of $Im([\chi]_{NDD})$ profiles associated with a more pronounced effect of NDD interaction, the parameters (R_1, R_2, and R_3) are set at the values same as those selected for Fig. 2. The only deviation is that the probe laser is detuned at a value of 4.2 MHz. In the absence of the travelling-wave field (R_{10}) and $\phi = 0$, two sphere-like structures of the 3D probe absorption emerge in two different subspaces $(\pm x, \pm y, \pm z)$ (Fig. 3a). The substantial modification in the spatial

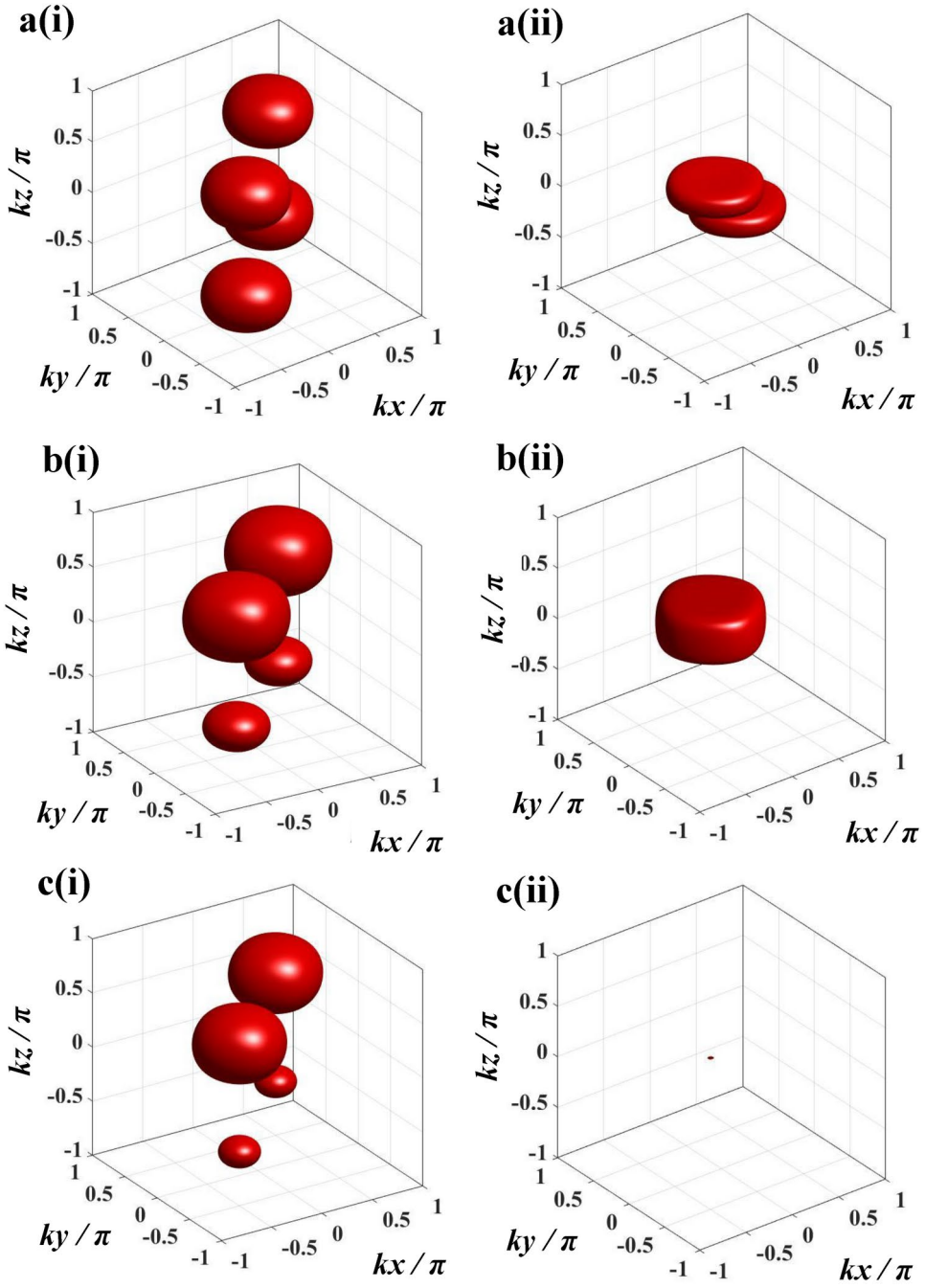

Fig. 2. 3D isosurface plots of the space-dependent probe absorption for the scheme -I with isovalue = 0.6. (**a**) $R_{10} = 0$, $\phi = 0$; (**b**) $R_{10} = 0.314$ MHz, $\phi = 0$; (**c**) $R_{10} = 0.314$ MHz, $\phi = 0.1755\pi$. Other common parameters: $R_1 = R_2 = 1.6$ MHz, $R_3 = 1.13$ MHz, $\Delta_p = \Delta_1 = \Delta_2 = 0$. The figures with notations (i) of the left panel and (ii) of the right panel correspond to the cases of probe absorption without employing the NDD effect and in the presence of the NDD effect with $C = 6$, respectively.

pattern of probe absorption may be attributed to the increase in the NDD parameter associated with the non-zero value of probe detuning when compared to the localization structure shown in Fig. 2a(ii). When the phase ϕ is set at a value of 0.219π, a notable change is induced in the localization patterns (Fig. 3b) displaying a prominent decrease in their sizes. This modification in isosurface plots shows a strong dependence of $Im([\chi]_{NDD})$ on ϕ in view of obtaining high-resolution 3D atom localization. In this case, the spatial resolution of a sphere-like isosurface is found $\frac{\lambda^3}{3.2\times10^6}$ (approx.) ($\lambda/161$, $\lambda/200$, and $\lambda/100$ along the x-, y-, and z- directions, respectively).

To explore the impact of R_{10} on the localization surfaces, we apply the travelling-wave field with the magnitude $R_{10} = 0.001$ MHz without affecting other parameters and show the corresponding isosurface profile in Fig. 3c. The tiny sphere-like pattern in the (x, y, z) subspace with its centre at ($kx/\pi = 0.5$, $ky/\pi = 0.5$, $kz/\pi = 0.5$)

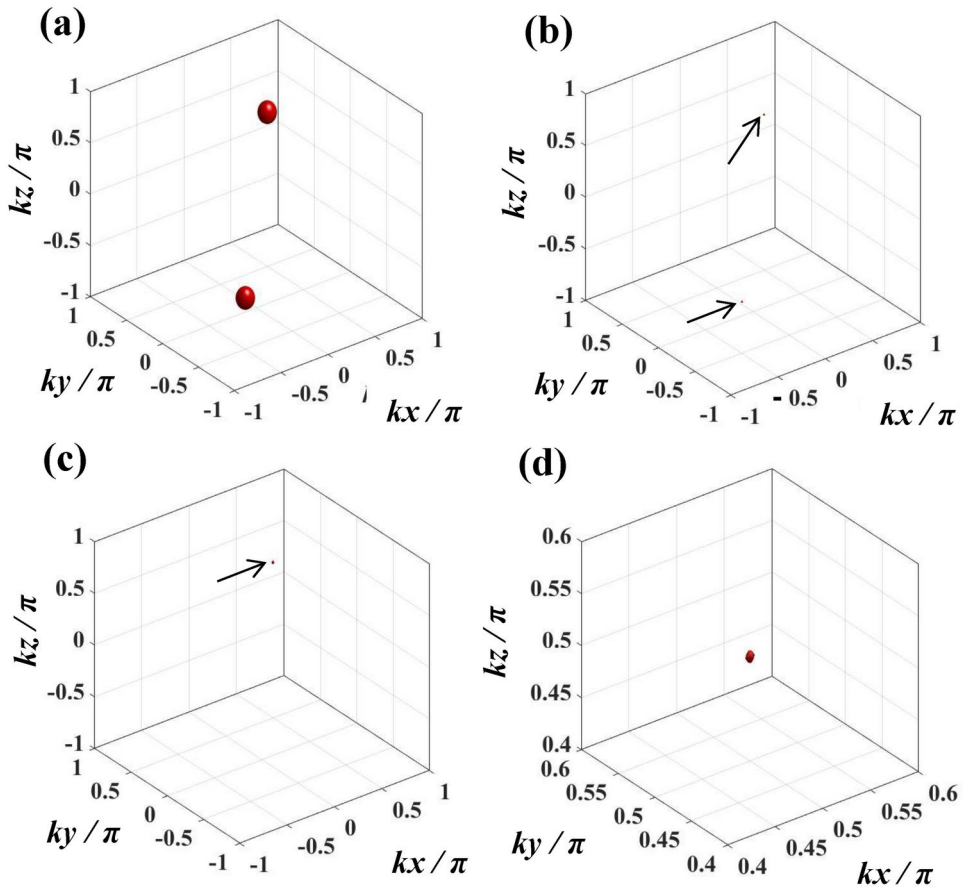

Fig. 3. 3D isosurface plots of the space-dependent probe absorption in the presence of the NDD effect for the scheme -I with isovalue = 0.6. (**a**) $R_{10} = 0$, $\phi = 0$; (**b**) $R_{10} = 0$, $\phi = 0.219\pi$; (**c**) $R_{10} = 0.001$ MHz, $\phi = 0.219\pi$; (**d**) $R_{10} = 0.001$ MHz, $\phi = 0.221\pi$. Other common parameters: $C = 9$, $R_1 = R_2 = 1.6$ MHz, $R_3 = 1.13$ MHz, $\Delta_p = 4.2$ MHz, $\Delta_1 = \Delta_2 = 0$.

experiences a very small increase in size, while the other pattern in the $(-x, -y, -z)$ subspace disappears in comparison to the localization patterns as shown in Fig. 3b. This feature indicates the attainment of 100% detection probability of the atom in the central position of the first octant (x, y, z) with the limit of spatial resolution $\frac{\lambda^3}{1.2\times10^6}$ (approx.) ($\lambda/100$, $\lambda/161$, and $\lambda/73$ along the x-, y-, and z- directions, respectively). In an attempt to achieve the maximum resolution in detecting atoms, we have further tuned ϕ to a value of 0.221π and displayed the corresponding isosurface plot in Fig. 3d. Tuning the system at the given value of the phase leads to the presence of a very tiny sphere-like localization structure with the same coordinate values. In this case, the ultra-high-resolution 3D localization with the 100% probability of finding the atom within a sub-half-wavelength range is made plausible when we obtain from Fig. 3d that the spatial extent of the localized structure becomes $\Delta(kx/\pi) \approx 0.0098$, $\Delta(ky/\pi) \approx 0.0049$, and $\Delta(kz/\pi) \approx 0.012$. These magnitudes indicate that the degree of localization with the limit of spatial resolution is nearly $\frac{\lambda^3}{13.6\times10^6}$ ($\lambda/204$, $\lambda/408$, and $\lambda/164$ along the x-, y-, and z- directions, respectively).

In the subsequent discussion, we delve into examining how the space-dependent field configurations, along with the system parameters of the scheme-II, affect the localization behaviours of atoms in three dimensions. This scheme is different from the scheme-I in the aspect that the space-dependent field arrangements $R_1(z)$ and $R_2(x, y)$ of the scheme-I experience a role-reversal of the standing-wave field arrangements ($R_2(z)$ and $R_1(x, y)$) in the scheme-II. A travelling wave (R_{10}) is also applied with the field of Rabi frequency $R_1(x, y)$. Here also in Fig. 4, like Fig. 2 for the scheme-I, we have presented the NDD-effect-induced 3D probe absorption ($Im([\chi]_{NDD})$) isosurfaces for the NDD-parameter value ($C = 3$) in the right panel whereas the 3D probe absorption ($Im(\chi_o)$) isosurfaces in the left panel without employing the NDD effect. To plot the localization characteristics in Fig. 4, we set the parameters as $R_1 = R_2 = 1.5$ MHz, $R_3 = 1.2$ MHz, $\Delta_p = \Delta_1 = \Delta_2 = 0$. In the absence of any travelling-wave field, Fig. 4a(i) and (ii) exhibit localization patterns for $\phi = 0$. Fig. 4a(i) and (ii), respectively, replicate the similar natures of 3D variation of probe absorption like Fig. 2a(i) and (ii) in the absence and presence of the NDD effect. However, the localization volumes of the isosurfaces shown in Fig. 4a(i) and (ii) are significantly smaller than those of the isosurfaces drawn in Fig. 2a(i) and (ii). In comparison to the isosurface profile, as shown in Fig. 2b(i), the spatial variation of the plotted isosurface in Fig. 4b(i) changes drastically. Two oblate spheroids evolve in the (x, y, z) and $(x, y, -z)$ subspaces, as shown in Fig. 4b(i). This highly contrastive

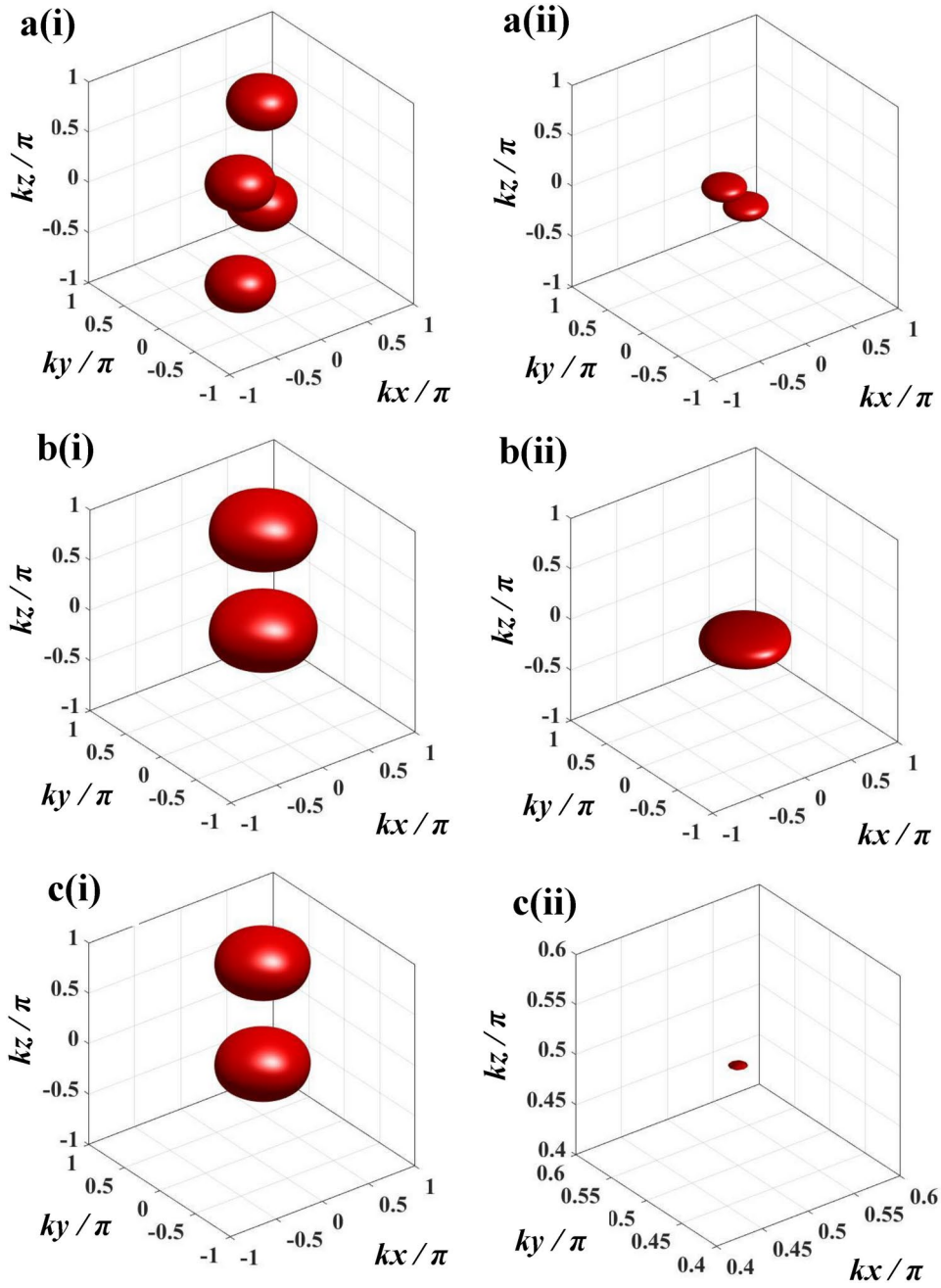

Fig. 4. 3D isosurface plots of the space-dependent probe absorption for the scheme-II with isovalue = 0.6. (**a**) $R_{10} = 0$, $\phi = 0$; (**b**) $R_{10} = 0.8$ MHz, $\phi = 0$; (**c**) $R_{10} = 0.8$ MHz, $\phi = 0.8417\pi$. Other common parameters: $R_1 = R_2 = 1.5$ MHz, $R_3 = 1.2$ MHz, $\Delta_p = \Delta_1 = \Delta_2 = 0$. The figures with notations (i) of the left panel and (ii) of the right panel correspond to the cases of probe absorption without employing the NDD effect and in the presence of the NDD effect with $C = 3$, respectively.

modification occurs due to the application of the travelling-wave field with the Rabi frequency value, $R_{10} = 0.8$ MHz, which is greater than that considered for Fig. 2b(i). Under the influence of the NDD interaction, the isosurface profile of Fig. 4b(i) is transformed into a flat disc-like isosurface in the $(x, y, -z)$ subspace as shown in Fig. 4b(ii). The reduction of the size of the localization structure in Fig. 4b(ii) is prominent when compared to that of the localization pattern presented in Fig. 2b(ii). This feature confirms the signature of 100% probability of finding the atom in the $(x, y, -z)$ subspace. We set the collective-phase parameter (ϕ) at a value of 0.8417π and display the phase-induced spatial variation of the localization profile in Fig. 4c(i) and (ii). So far as the value of ϕ is concerned, we have observed a marked distinction in the isosurfaces without (Fig. 4c(i)) and with (Fig. 4c(ii)) the NDD effect. The impact of the value of ϕ on the isosurfaces is very insignificant in Fig. 4c(i), leading to only a slight decrement in localization volumes. In the presence of the same value of ϕ, the occurrence of a tiny flat disc-like structure in the (x, y, z) subspace, as prominent in Fig. 4c(ii), indicates a

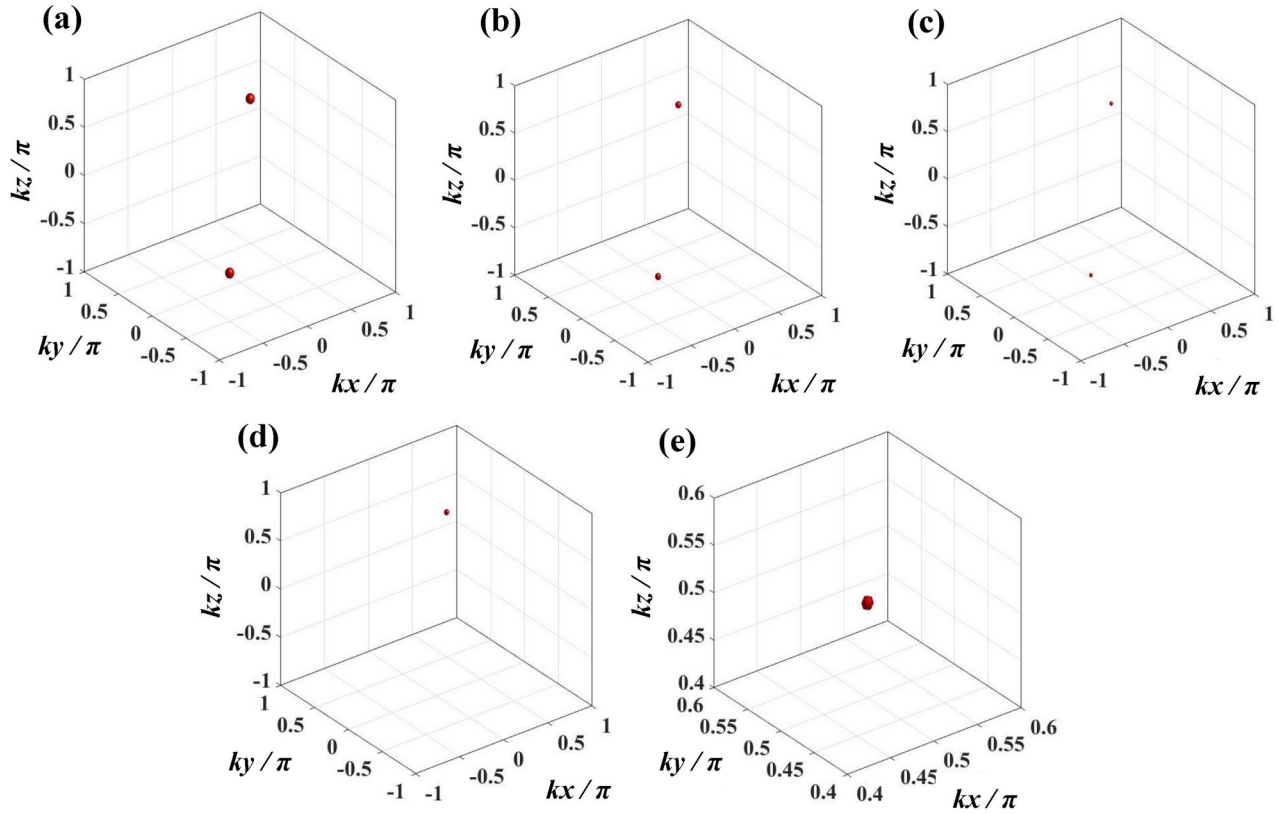

Fig. 5. 3D isosurface plots of the space-dependent probe absorption in the presence of the NDD effect for the scheme-II with isovalue = 0.6. (**a**) $R_{10} = 0$, $\Delta_p = 3.2$ MHz, $\phi = 0$; (**b**) $R_{10} = 0$, $\Delta_p = 3.2$ MHz, $\phi = 0.08\pi$; (**c**) $R_{10} = 0$, $\Delta_p = 3.2$ MHz, $\phi = 0.098\pi$; (**d**) $R_{10} = 0.00193$ MHz, $\Delta_p = 3.2$ MHz, $\phi = 0.098\pi$; (**e**) $R_{10} = 0.00193$ MHz, $\Delta_p = 3.205$ MHz, $\phi = 0.098\pi$. Other common parameters: $C = 8$, $R_1 = R_2 = 1.5$ MHz, $R_3 = 1.2$ MHz, $\Delta_1 = \Delta_2 = 0$.

significant improvement in the precision as well as the resolution of atom localization as a direct consequence of the NDD effect. Thus, the 100% detection probability of the atom in the sub-half-wavelength domain of 3D space is assured with a significant enhancement in the precision and spatial resolution. The spatial limit of resolution for this localization pattern corresponds to the localization volume of $\frac{\lambda^3}{2.8\times10^6}$ (λ/14, λ/200, and λ/1000 along the *x*-, *y*- and *z*- axes, respectively).

Lastly, we discuss the features of 3D localization isosurface profiles presented in Fig. 5a–e for the scheme-II. We set the parameter condition (R_1, R_2, and R_3) of Fig. 5 the same as those set for Fig. 4 except the NDD parameter value ($C = 8$) and probe detuning $\Delta_p = 3.2$ MHz (Fig. 5a–d). So far as 3D localization is concerned, it is evident that Fig. 5a,b are almost similar to Fig. 3a,b, respectively. In the case of Fig. 5b, we set the phase $\phi = 0.08\pi$, whereas Fig. 5a is plotted with $\phi = 0$. In contrast to the localization structure shown in Fig. 5b, the spatial volumes of two sphere-like isosurfaces in the $(\pm x, \pm y, \pm z)$ subspaces get sufficiently decreased (See Fig. 5c) when the system is tuned for $\phi = 0.098\pi$. To attain the maximum detection probability, we have resorted to the application of R_{10} with a value of 0.00193 MHz and plot the corresponding isosurface profile in Fig. 5d. In this case, only the spherical pattern of localization in the (*x*, *y*, *z*) subspace persists at the position (0.5, 0.5, 0.5) accompanied by the disappearance of the other pattern in the $(-x, -y, -z)$ subspace ensuring the 100% probability of detecting the atom in the sub-half-wavelength domain. The limit of the spatial resolution leads to the order of $\frac{\lambda^3}{1.5\times10^5}$ (approx.) (λ/59, λ/67, and λ/38 along the *x*-, *y*- and *z*- axes, respectively). To demonstrate the realization of 3D atom localization with ultra-high resolution in the present scheme, we tune the probe detuning at $\Delta_p = 3.205$ MHz and show the appearance of a very tiny sphere-like singular structure of localization at (0.5, 0.5, 0.5) in the isosurface plot of Fig. 5e. The very small spatial volume of the isosurface in the sub-half-wavelength domain signifies the 100% detection probability of atoms with the spatial extent of resolution ($\Delta(kx/\pi) \approx 0.01$, $\Delta(ky/\pi) \approx 0.0054$, and $\Delta(kz/\pi) \approx 0.0152$. Based on these values the limit of spatial resolution is estimated nearly $\frac{\lambda^3}{9.7\times10^6}$ (λ/200, λ/370, and λ/132 along the *x*-, *y*- and *z*- axes, respectively) in this scheme. This is to mention here that the collective phase can be easily controlled by using a phase-locked technique[63,64] for possible experimentation. In our chosen parameters' regime, we have shown the appearance of a single localization structure in the sub-half-wavelength domain with ultra-high spatial resolution for both schemes.

To get physical insights into how field-induced quantum interference affects and modifies the evolution of spatial distributions of 3D localization patterns, as shown in Figs. 2, 3, 4 snd 5, we note that, for any value of ϕ (other than $\pi/2$), the expression of space-dependent probe susceptibility (χ_o) indicates the appearance of *explicit* quantum interference effect due to the presence of the product term of space-dependent and space-independent Rabi frequencies in the denominator of the expression of ρ_{21}. The interference term is found to be modulated by the collective phase coherence term. In the presence of Rabi frequency of the travelling-wave field R_{10} in the expression of $R_1(x, y, z)$, the $|R_1^2(x, y, z)|$ term contributes to the *implicit* interference effect through the terms $R_{10}R_1$ *sin*(*kz*) and $R_{10}R_1$ (*sin*(*kx*) + *sin*(*ky*)) for the schemes I and II, respectively. When the travelling-wave field (R_{10}) is incorporated into the system, the 3D localization features appear as a result of the competitive nature of the variations of the *implicit* and *explicit* interference effects. As $[\chi]_{NDD}$ relates nonlinearly with χ_o, the combined effect of such quantum interference mechanisms becomes further modulated as a consequence of the NDD effect. Thus, in our work, the properly tuned NDD parameter with other system parameters plays a pivotal role in shaping 3D localization patterns leading to ultra-high resolution.

Conclusion

In conclusion, we have presented a novel method for precise 3D atom localization by observing the spatial variation of NDD effect-induced absorption of a weak probe field in a partially closed four-level Y-type atomic system. Under the resonant interaction of the atom with the standing and travelling-wave fields, we have shown how the NDD effect with appropriate adjustment of the system parameters (Rabi frequencies, probe detuning, and collective phase) allows us to efficiently control the 3D localization patterns of the atom. Our findings suggest that, within our framework, the 100% detection probability of the atom can be realized with a spatial resolution limit having a localization volume nearly of the order of $(\lambda/100)^3$. The work shows significant potential for its applications in atom nanolithography and atom imaging, which will be useful in quantum information processing and technology in the near future.

Data Availability

All data generated or analysed during this study are included in this published article.

Received: 25 September 2024; Accepted: 17 March 2025
Published online: 20 August 2025

References

1. Metcalf, H. & Van der Straten, P. Cooling and trapping of neutral atoms. *Phys. Rep.* **244**, 203 (1994).
2. Phillips, W. D. Nobel lecture: Laser cooling and trapping of neutral atoms. *Rev. Mod. Phys.* **70**, 721 (1998).
3. Collins, G. P. Experimenters produce new Bose-Einstein condensate(s) and possible puzzles for theorists. *Phys. Today* **49**, 18 (1996).
4. Wu, Y., Yang, X. X. & Sun, C. P. Systematic method to study the general structure of Bose–Einstein condensates with arbitrary spin. *Phys. Rev. A* **62**, 063603 (2000).
5. Gorshkov, A. V., Jiang, L., Greiner, M., Zoller, P. & Lukin, M. D. Coherent quantum optical control with subwavelength resolution. *Phys. Rev. Lett.* **100**, 093005 (2008).
6. Johnson, K. S. et al. Localization of metastable atom beams with optical standing waves: nanolithography at the heisenberg limit. *Science* **280**, 1583 (1998).
7. Boto, A. N. et al. Quantum interferometric optical lithography: exploiting entanglement to beat the diffraction limit. *Phys. Rev. Lett.* **85**, 2733 (2000).
8. Storey, P. & Collett, M. Atomic-position resolution by quadrature-field measurement. *Phys. Rev. A* **47**, 405 (1993).
9. Quadt, R., Collett, M. & Walls, D. F. Measurement of atomic motion in a standing light eld by homodyne detection. *Phys. Rev. Lett.* **74**, 351 (1995).
10. Rempe, G. One atom in an optical cavity: Spatial resolution beyond the standard diffraction limit. *Appl. Phys. B* **60**, 233 (1995).
11. Rudy, P., Ejnisman, R. & Bigelow, N. P. Fluorescence investigation of parametrically excited motional wave packets in optical lattices. *Phys. Rev. Lett.* **78**, 4906 (1997).
12. Paspalakis, E. & Knight, P. L. Localizing an atom via quantum interference. *Phys. Rev. A* **63**, 065802 (2001).
13. Qamar, S., Zhu, S. Y. & Zubairy, M. S. Atom localization via resonance fluorescence. *Phys. Rev. A* **61**, 063806 (2000).
14. Ghafoor, F., Qamar, S. & Zubairy, M. S. Atom localization via phase and amplitude control of the driving field. *Phys. Rev. A* **65**, 043819 (2002).
15. Sahrai, M., Tajalli, H., Kapale, K. T. & Zubairy, M. S. Subwavelength atom localization via amplitude and phase control of the absorption spectrum. *Phys. Rev. A* **72**, 013820 (2005).
16. Liu, C., Gong, S. Q., Cheng, D., Fan, X. & Xu, Z. Atom localization via interference of dark resonances. *Phys. Rev. A* **73**, 025801 (2006).
17. Qamar, S., Mehmood, A. & Qamar, Sh. Subwavelength atom localization via coherent manipulation of the Raman gain process. *Phys. Rev. A* **79**, 033848 (2009).
18. Agarwal, G. S. & Kapale, K. T. Subwavelength atom localization via coherent population trapping. *J. Phys. B* **39**, 3437 (2006).
19. Proite, N. A., Simmons, Z. J. & Yavuz, D. D. Observation of atomic localization using electromagnetically induced transparency. *Phys. Rev. A* **83**, 041803(R) (2011).
20. Wang, Z. & Jiang, J. Sub-half-wavelength atom localization via probe absorption spectrum in a four-level atomic system. *Phys. Lett. A* **374**, 4853 (2010).
21. Dutta, B. K., Panchadhyayee, P. & Mahapatra, P. K. Precise localization of a two-level atom by the superposition of two standing wave fields. *J. Opt. Soc. Am. B* **29**, 3299 (2012).
22. Evers, J., Qamar, S. & Zubairy, M. S. Atom localization and center-of-mass wave-function determination via multiple simultaneous quadrature measurements. *Phys. Rev. A* **75**, 053809 (2007).
23. Jin, L., Sun, H., Niu, Y., Jin, S. & Gong, S. Q. Two-dimension atom nano-lithograph via atom localization. *J. Mod. Opt.* **56**, 805 (2009).
24. Ivanov, V. & Rozhdestvensky, Y. Two-dimensional atom localization in a four-level tripod system in laser field. *Phys. Rev. A* **81**, 033809 (2010).
25. Ding, C., Li, J. H., Yang, X., Zhan, Z. & Liu, J.-B. Two-dimensional atom localization via a coherence-controlled absorption spectrum in an N-tripod-type five-level atomic system. *J. Phys. B: At. Mol. Opt. Phys.* **44**, 145501 (2011).

26. Wan, R. G., Kou, J., Jiang, L., Jiang, Y. & Gao, J. Y. Two-dimensional atom localization via controlled spontaneous emission from a driven tripod system. *J. Opt. Soc. Am. B* **28**, 10 (2011).
27. Wan, R. G., Kou, J., Jiang, L., Jiang, Y. & Gao, J. Y. Two-dimensional atom localization via quantum interference in a coherently driven inverted-Y system. *Opt. Commun.* **284**, 985 (2011).
28. Wan, R. G., Kou, J., Jiang, L., Jiang, Y. & Gao, J. Y. Two-dimensional atom localization via interacting double-dark resonances. *J. Opt. Soc. Am. B* **28**, 622 (2011).
29. Ding, C., Li, J. H., Zhan, Z. & Yang, X. Two-dimensional atom localization via spontaneous emission in a coherently driven five-level M-type atomic system. *Phys. Rev. A* **83**, 063834 (2011).
30. Ding, C., Li, J. H., Yang, X., Zhang, D. & Xiong, H. Proposal for efficient two-dimensional atom localization using probe absorption in a microwave-driven four-level atomic system. *Phys. Rev. A* **84**, 043840 (2011).
31. Li, J. H., Yu, R., Liu, M., Ding, C. & Yang, X. Efficient two-dimensional atom localization via phase sensitive absorption spectrum in a radio-frequency-driven four-level atomic system. *Phys. Lett. A* **375**, 3978–3985 (2011).
32. Ding, C., Li, J., Yu, R., Hao, X. & Wu, Y. High-precision atom localization via controllable spontaneous emission in a cycle-configuration atomic system. *Opt. Express* **20**, 7870 (2012).
33. Wang, Z. et al. Atom localization via controlled spontaneous emission in a five-level atomic system. *Ann. Phys.* **327**, 1132–1145 (2012).
34. Rahmatullah, & Qamar, S. Two-dimensional atom localization via probe-absorption spectrum. *Phys. Rev. A* **88**, 013846 (2013).
35. Wu, J. C. & Ai, B. Q. Two-dimensional sub-wavelength atom localization in an electromagnetically induced transparency atomic system. *Eur. Phys. Lett.* **107**, 14002 (2014).
36. Shui, T., Wang, Z. & Yu, B. Efficient two-dimensional atom localization via spontaneously generated coherence and incoherent pump. *J. Opt. Soc. Am. B* **32**, 210 (2015).
37. Shui, T., Wang, Z., Cao, Z. & Yu, B. Two-dimensional sub-half-wavelength atom localization via Autler–Townes microscopy. *Laser Phys.* **24**, 055202 (2014).
38. Wang, Z., Shui, T. & Yu, B. Efficient two-dimensional atom localization in a four-level atomic system beyond weak-probe approximation. *Opt. Commun.* **313**, 263 (2014).
39. Panchadhyayee, P., Dutta, B. K., Bayal, I., Das, N. & Mahapatra, P. K. Field-induced superposition effects on atom localization via resonance fluorescence spectrum. *Phys. Scr.* **94**, 105104 (2019).
40. Idrees, M., Ullah, M., Bacha, B. A., Ullah, A. & Wang, L.-G. High-resolution two-dimensional atomic microscopy in a tripod-type four-level atomic medium via standing wave fields. *Laser Phys.* **30**, 115402 (2020).
41. Idrees, M., Kalsoom, H., Bacha, B. A., Ullah, A. & Wang, L.-G. Spatial-dependent probe transmission based high-precision two-dimensional atomic localization. *Commun. Theor. Phys.* **73**, 045102 (2021).
42. Idrees, M. & Khan, Z. A. Phase-sensitive manipulation of atom localization using probe field transmission spectrum. *Opt. Quant. Electron.* **55**, 1247 (2023).
43. Idrees, M., Ullah, M., Bacha, B. A., Ullah, A. & Wang, L.-G. High-resolution two-dimensional atomic localization via tunable surface plasmon polaritons. *Plasmonics* **16**, 1773 (2021).
44. Qi, Y. H., Zhou, F. X., Huang, T., Niu, Y. P. & Gong, S. Q. J. Mod. Opt. *Three-dimensional atom localization in a five-level M-type atomic system* **59**, 1092 (2012).
45. Ivanov, V. S., Rozhdestvensky, Y. V. & Suominen, K. A. Three-dimensional atom localization by laser fields in a four-level tripod system. *Phys. Rev. A* **90**, 063802 (2014).
46. Wang, Z. & Yu, B. Efficient three-dimensional atom localization via probe absorption. *J. Opt. Soc. Am. B* **32**, 1281–1286 (2015).
47. Wang, Z., Cao, D. & Yu, B. Three-dimensional atom localization via electromagnetically induced transparency in a three-level atomic system. *Appl. Opt.* **55**, 3582 (2016).
48. Hamedi, H. R. & Mehmannavaz, M. R. Phase control of three-dimensional atom localization in a four-level atomic system in Lambda configuration. *J. Opt. Soc. Am. B* **33**, 41 (2016).
49. Zhu, Z., Chen, A.-X., Liu, S. & Yang, W.-X. High-precision three-dimensional atom localization via three-wave mixing in V-type three-level atoms. *Phys. Lett. A* **33**, 3956 (2016).
50. Wang, Z. & Yu, B. High-precision three-dimensional atom localization via spontaneous emission in a four-level atomic system. *Laser Phys. Lett.* **13**, 065203 (2016).
51. Zhu, Z. et al. Three-dimensional atom localization from spatial interference in a double two-level atomic system. *Phys. Rev. A* **94**, 013826 (2016).
52. Yang, L., Cao, D., Wang, Y., Wang, Z. & Yu, B. Three-dimensional sub-half-wavelength atom localization via interacting double-dark resonances. *Laser Phys.* **26**, 115501 (2016).
53. Wang, Z. & Yu, B. Precision localization of single atom via phase-dependent quantum coherence in three dimensions. *Laser Phys. Lett.* **13**, 035501 (2016).
54. Wang, Z., Song, F., Chen, J. & Yu, B. Coherent control of three-dimensional atom localization based on different coupled mechanisms. *Quantum Inf. Process.* **16**, 129 (2017).
55. Mao, Y. & Wu, J. High-precision three-dimensional atom localization in a microwave-driven atomic system. *J. Opt. Soc. Am. B* **34**, 1070 (2017).
56. Chen, J., Song, F., Wang, Z. & Yu, B. Three-dimensional atom localization via spontaneous emission from two different decay channels. *Laser Phys. Lett.* **15**, 065205 (2018).
57. Zhang, D., Yu, R., Sun, Z., Ding, C. & Zubairy, M. S. High-precision three-dimensional atom localization via phase-sensitive absorption spectra in a four-level atomic system. *J. Phys. B: At. Mol. Opt. Phys.* **51**, 025501 (2018).
58. Panchadhyayee, P., Dutta, B. K., Das, N. & Mahapatra, P. K. Resonance fluorescence microscopy via three-dimensional atom localization. *Quantum Inf. Process.* **17**, 20 (2018).
59. Song, F., Chen, J.-Y., Wang, Z.-P. & Yu, B.-L. Three-dimensional atom localization via spontaneous emission in a four-level atom. *Front. Phys.* **13**, 134208 (2018).
60. Zhang, D., Yu, R., Sun, Z., Ding, C. & Zubairy, M. S. Efficient three-dimensional atom localization using probe absorption in a diamond configuration atomic system. *J. Phys. B: At. Mol. Opt. Phys.* **52**, 035502 (2019).
61. Song, F., Wang, Z., Juan, R. & Yu, B. Atom localization in five level atomic system driven by an additional incoherent pump. *Appl. Phys. B* **125**, 69 (2019).
62. Bowden, C. M. & Dowling, J. P. Near-dipole-dipole effects in dense media: Generalized Maxwell–Bloch equations. *Phys. Rev. A* **47**, 1247 (1993).
63. Dowling, J. P. & Bowden, C. M. Near dipole-dipole effects in lasing without inversion: An enhancement of gain and absorptionless index of refraction. *Phys. Rev. Lett.* **70**, 1421 (1993).
64. Manka, A. S., Dowling, J. P., Bowden, C. M. & Fleischhauer, M. A review of local field effects in lasing without inversion. *Quantum Opt.* **6**, 371 (1994).
65. Agarwal, G. S. & Robert, W. Boyd, Elimination of the band gap of a resonant optical material by electromagnetically induced transparency. *Phys. Rev. A* **60**, R2681 (1999).
66. Meystre, P. & Sargent, M. *Elements of Quantum Optics* 3rd edn. (Springer, Berlin, 1999).
67. Panchadhyayee, P., Banerjee, A. & Dutta, B. K. Vortex beam induced spatial modulation of quantum-optical effects in a coherent atomic medium. *J. Phys. B: At. Mol. Opt. Phys.* **57**, 105402 (2024).
68. Jackson, J. D. *Classical Electrodynamics* 3rd edn. (New Jersy, Wiley, 1999).

69. Noh, H.-R. & Moon, H. S. Discrimination of one-photon and two-photon coherence parts in electromagnetically induced transparency for a ladder-type three-level atomic system. *Opt. Express* **19**, 11128 (2011).
70. Bordonalli, A. C., Walton, C. & Seeds, A. J. High-performance phase locking of wide linewidth semiconductor lasers by combined use of optical injection locking and optical phase-lock loop. *J. Lightwave Technol.* **12**, 328 (1999).
71. Appel, J., MacRae, A. & Lvovsky, A. I. A versatile digital GHz phase lock for external cavity diode lasers. *Meas. Sci. Technol.* **20**, 055302 (2009).

Acknowledgements
PP thankfully acknowledges the Research Centre in Natural Sciences of PKC for support. BKD likes to acknowledge the tenure of his service in J. K. College, Purulia, because he felt the motivation to do research in this direction during this period.

Author contributions
BKD devised the basic model and jointly with AB and PP established the final framework. PP performed simulations. All the authors contributed to writing and editing of the manuscript.

Funding
We have no funding behind the research work.

Declarations

Competing Interests
The authors declare that they have no competing interests.

Additional information
Supplementary Information The online version contains supplementary material available at https://doi.org/10.1038/s41598-025-94788-3.

Correspondence and requests for materials should be addressed to P.P. or B.K.D.

Reprints and permissions information is available at www.nature.com/reprints.

Publisher's note Springer Nature remains neutral with regard to jurisdictional claims in published maps and institutional affiliations.